The Astrophysical Journal Letters, 880:L17 (15pp), 2019 July 20 https://doi.org/10.3847/2041-8213/ab2988

TESS Hunt for Young and Maturing Exoplanets (THYME): A Planet in the 45 Myr Tucana–Horologium Association

Elisabeth R. Newton[1,2], Andrew W. Mann[3], Benjamin M. Tofflemire[4], Logan Pearce[4], Aaron C. Rizzuto[4,26], Andrew Vanderburg[4,27], Raquel A. Martinez[4], Jason J. Wang[5,26], Jean-Baptiste Ruffio[6], Adam L. Kraus[4], Marshall C. Johnson[7], Pa Chia Thao[3], Mackenna L. Wood[3], Rayna Rampalli[8], Eric L. Nielsen[6], Karen A. Collins[9], Diana Dragomir[10], Coel Hellier[11], D. R. Anderson[11], Thomas Barclay[12,13], Carolyn Brown[14], Gregory Feiden[15], Rhodes Hart[16], Giovanni Isopi[17], John F. Kielkopf[18], Franco Mallia[17], Peter Nelson[19], Joseph E. Rodriguez[9], Chris Stockdale[20], Ian A. Waite[16], Duncan J. Wright[14], Jack J. Lissauer[21], George R. Ricker[2], Roland Vanderspek[2], David W. Latham[9], S. Seager[2,22,23], Joshua N. Winn[24], Jon M. Jenkins[21], Luke G. Bouma[24], Christopher J. Burke[2], Misty Davies[21], Michael Fausnaugh[2], Jie Li[21,25], Robert L. Morris[21,25], Koji Mukai[12,13], Joel Villaseñor[2], Steven Villeneuva[2], Robert J. De Rosa[6], Bruce Macintosh[6], Matthew W. Mengel[14], Jack Okumura[14], and Robert A. Wittenmyer[14]

[1] Department of Physics and Astronomy, Dartmouth College, Hanover, NH 03755, USA; Elisabeth.R.Newton@Dartmouth.edu
[2] Department of Physics and Kavli Institute for Astrophysics and Space Research, Massachusetts Institute of Technology, Cambridge, MA 02139, USA
[3] Department of Physics and Astronomy, The University of North Carolina at Chapel Hill, Chapel Hill, NC 27599, USA
[4] Department of Astronomy, The University of Texas at Austin, Austin, TX 78712, USA
[5] Department of Astronomy, California Institute of Technology, Pasadena, CA 91125, USA
[6] Kavli Institute for Particle Astrophysics and Cosmology, Stanford University, Stanford, CA 94305, USA
[7] Department of Astronomy, The Ohio State University, Columbus, OH 43210, USA
[8] Department of Astronomy, Columbia University, 550 West 120th Street, New York, NY 10027, USA
[9] Center for Astrophysics Harvard and Smithsonian, 60 Garden Street, Cambridge, MA 02138, USA
[10] Kavli Institute for Astrophysics and Space Science, Massachusetts Institute of Technology, Cambridge, MA 02139, USA
[11] Astrophysics Group, Keele University, Staffordshire ST5 5BG, UK
[12] NASA Goddard Space Flight Center, 8800 Greenbelt Road, Greenbelt, MD 20771, USA
[13] University of Maryland, Baltimore County, 1000 Hilltop Circle, Baltimore, MD 21250, USA
[14] University of Southern Queensland, Centre for Astrophysics, West Street, Toowoomba, QLD 4350 Australia
[15] Department of Physics, University of North Georgia, Dahlonega, GA 30597, USA
[16] Centre for Astrophysics, University of Southern Queensland, Toowoomba, QLD 4350, Australia
[17] Campo Catino Astronomical Observatory, Regione Lazio, Guarcino (FR), I-03010, Italy
[18] Department of Physics and Astronomy, University of Louisville, Louisville, KY 40292, USA
[19] Ellinbank Observatory, Australia
[20] Hazelwood Observatory, Australia
[21] NASA Ames Research Center, Moffett Field, CA 94035, USA
[22] Department of Earth, Atmospheric and Planetary Sciences, Massachusetts Institute of Technology, Cambridge, MA 02139, USA
[23] Department of Aeronautics and Astronautics, MIT, 77 Massachusetts Avenue, Cambridge, MA 02139, USA
[24] Department of Astrophysical Sciences, Princeton University, 4 Ivy Lane, Princeton, NJ 08544, USA
[25] SETI Institute, Mountain View, CA 94043, USA
Received 2019 April 22; revised 2019 June 7; accepted 2019 June 11; published 2019 July 23

Abstract

Young exoplanets are snapshots of the planetary evolution process. Planets that orbit stars in young associations are particularly important because the age of the planetary system is well constrained. We present the discovery of a transiting planet larger than Neptune but smaller than Saturn in the 45 Myr Tucana–Horologium young moving group. The host star is a visual binary, and our follow-up observations demonstrate that the planet orbits the G6V primary component, DS Tuc A (HD 222259A, TIC 410214986). We first identified transits using photometry from the *Transiting Exoplanet Survey Satellite* (*TESS*; alerted as TOI 200.01). We validated the planet and improved the stellar parameters using a suite of new and archival data, including spectra from Southern Astrophysical Research/Goodman, South African Extremely Large Telescope/High Resolution Spectrograph and Las Cumbres Observatories/Network of Robotic Echelle Spectrographs; transit photometry from *Spitzer*; and deep adaptive optics imaging from Gemini/Gemini Planet Imager. No additional stellar or planetary signals are seen in the data. We measured the planetary parameters by simultaneously modeling the photometry with a transit model and a Gaussian process to account for stellar variability. We determined that the planetary radius is $5.70 \pm 0.17\ R_{\oplus}$ and that the orbital period is 8.1 days. The inclination angles of the host star's spin axis, the planet's orbital axis, and the visual binary's orbital axis are aligned within 15° to within the uncertainties of the relevant data. DS Tuc Ab is bright enough ($V = 8.5$) for detailed characterization using radial velocities and transmission spectroscopy.

Key words: open clusters and associations: individual (Tucana-Horologium) – planets and satellites: detection – planets and satellites: individual (HD 222259A) – planets and satellites: individual (TIC 410214986) – planets and satellites: individual (TOI 200.01)

[26] 51 Pegasi b Fellow.
[27] NASA Sagan Fellow.

1. Introduction

Exoplanets do not form with the properties with which we observe them today: migration and dynamical interactions change their orbital parameters, high-energy radiation from their host stars causes atmospheric mass loss, and gaseous planets contract as they cool. The demographics of field-age (typically >1 Gyr) exoplanetary systems offers one way to learn about the evolutionary history of exoplanets. For example, the gap in the observed radius distribution of close-in planets (between super-Earths and mini-Neptunes) has been used as a probe of photoevaporation and to constrain typical core compositions (Lopez 2017; Owen & Wu 2017); and Owen & Lai (2018) explained the dearth of close-in giant planets as the joint result of high-eccentricity migration and photoevaporation.

Observations of planets young enough to still be undergoing dynamical and atmospheric changes provide a more direct way to probe planetary evolution; and planets in young stellar associations are particularly useful because the ages of these systems are known more precisely and accurately than those of their counterparts in the galactic field. The typically close-orbiting planets discovered through transit and radial velocity (RV) surveys complement the constraints on planet formation beyond the snow line available from direct imaging (e.g., Brandt et al. 2014; Bowler et al. 2015; Clanton & Gaudi 2016; Nielsen et al. 2019). They are also likely to be young representatives of the field-age exoplanets on which planetary demographics studies are based.

RV programs have detected Jupiter-mass planets in young clusters (Quinn et al. 2012, 2014), but are hindered by the RV jitter exhibited by these young, active stars (e.g., Saar & Donahue 1997; Paulson et al. 2004). Thanks to its excellent photometric precision and wide-area coverage, *K2* yielded a surge of exoplanet discoveries around young stars via the transit method. This included planets in the Hyades (David et al. 2016a; Mann et al. 2016a), Upper Scorpius (David et al. 2016b; Mann et al. 2016b), Praesepe (Mann et al. 2017; Rizzuto et al. 2018; Livingston et al. 2019), and Taurus-Auriga (David et al. 2019) associations.

The *Transiting Exoplanet Survey Satellite* (*TESS*) will survey 80% of the sky during its prime mission, with a focus on bright stars. *TESS* enables the transit search for young exoplanets in associations to be substantially expanded; and motivates our collaboration, the *TESS* Hunt for Young and Maturing Exoplanets (THYME) Project.

TESS provides the first opportunity for extensive transit surveys of stars in young moving groups (YMGs). YMGs are dynamically unbound associations of stars that are identified based on their common motion through the galaxy. YMGs have ages $\lesssim$300 Myr; and probe a more continuous range of ages than do young stellar clusters (see e.g., Bell et al. 2015). The stellar environments in YMGs also differ from those found in high-density, longer-lasting star clusters such as Praesepe or Pleiades. These clusters are less compact, and therefore stellar dynamical interactions are less frequent; as a result, they may be more characteristic of the precursors of exoplanetary systems that orbit typical field stars. Dynamical studies indicate that stellar interactions in open clusters are unlikely to disrupt planetary systems (e.g., Bonnell et al. 2001; Adams et al. 2006), but milder impacts, such as changes in eccentricity, are possible (Spurzem et al. 2009). Finally, most known YMGs are substantially less distant than stellar clusters (see e.g., Gagné & Faherty 2018). This provides significant advantages for detailed characterization of the planets through techniques such as transmission spectroscopy and precise RV monitoring. We report the discovery (Figure 1) of a close-in, transiting planet with a radius in between those of Neptune and Saturn. The stellar host is the primary component of DS Tuc (DS Tuc A, HD 222259A), which is a member of the Tucana–Horologium (Tuc-Hor) YMG. DS Tuc was one of the original members of the Tucana association of co-moving stars identified by Zuckerman & Webb (2000). Tucana was soon identified as being physically associated with the Horologium association of active stars (Torres et al. 2000), and together they formed one of the first known YMGs.

DS Tuc is a visual binary (Torres 1988), consisting of a G6V primary and a K3V secondary (Torres et al. 2006) separated by 5″. Soderblom et al. (1998) suggested that the secondary (DS Tuc B, HD 222259B) is itself a short period binary based on RV variations, and Cutispoto et al. (2002) reported spectral types for the components of K3/4V and K5V but did not provide further information. As we will discuss in Section 3.2, our RV measurements demonstrate that DS Tuc B is not likely to be a short-period binary.

In Section 2 we present discovery data from *TESS* and follow-up photometry from *Spitzer*. We additionally present new high-resolution spectra and long-term photometric monitoring, and discuss archival high-resolution spectra. In Section 3 we update the stellar parameters, and analyze the RVs and stellar rotation. In Section 4, we investigate the overall DS Tuc system, including modeling of the binary star orbit, and searching for additional companions in high-contrast imaging and in the *TESS* transit data. We present the results of our transit analysis, including identifying the stellar host as DS Tuc A and assessing false-positive scenarios, in Section 5. We discuss the overall system architecture and prospects for future follow-up in Section 6 and briefly summarize our findings in Section 7.

2. Observations

2.1. Photometry

2.1.1. TESS

TESS was launched on 2018 April 18 and commenced science operations on 2018 July 25. *TESS* uses its four small (10 cm effective aperture) cameras to monitor 24° × 96° sectors of sky nearly continuously over 27 day campaigns. DS Tuc was observed in the first sector of science operations during late 2018 July and August and was pre-selected for fast (two minute) cadence observations because of its membership in the young Tucana–Horologium Moving Group.[28] After the *TESS* data were downlinked to Earth, they were processed by the Science Processing and Operations Center (SPOC) pipeline at NASA Ames (Jenkins 2015; Jenkins et al. 2016), which calibrated the *TESS* pixels, extracted light curves, de-blended light from nearby contaminating stars, removed common-mode systematic errors, high-pass filtered the light curve, and searched for transits. We used the pre-search data condition simple aperture photometry (PDC-SAP) light curve and systematics solution throughout this Letter, masking the time $1346.5 < t < 1350$, except in our transit injection and

[28] The target was requested as part of our Guest Investigator program GO11175 (PI: Mann), as well as by GO11176 (PI: Czekala) and GO11250 (PI: Walter).

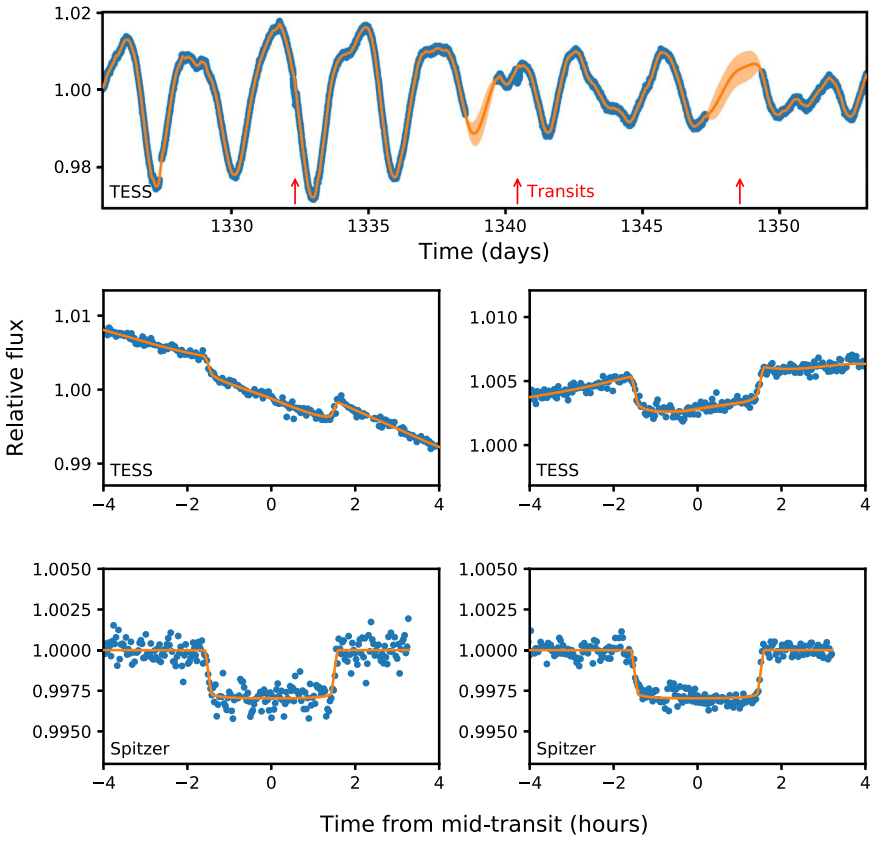

Figure 1. Discovery data from *TESS*, after our iterative flare rejection algorithm has been applied, and follow-up data from *Spitzer*. Data are shown as blue points; data for *Spitzer* are the means of 250 equally spaced bins. The top panel shows the full *TESS* light curve and the stellar variability Gaussian process (GP) model. The middle panel shows a zoom-in on the two transits observed with *TESS*. The bottom panel shows the two *Spitzer* transits at 4.5 μm. The best-fitting model from our joint fit to the these light curves is shown in orange; in this analysis we simultaneously model stellar variability in *TESS*, using a GP, and the transit parameters. The mean of the Markov chain Monte Carlo (MCMC) samples is shown as the opaque orange line; the 1σ deviations are shown as the semi-transparent orange region.

recovery tests (Section 4.4). This time corresponds to the loss of fine guiding, where t is given in *TESS* barycentric Julian date (BJD −2,457,000.0).

SPOC used the Transiting Planet Search module (TPS) to search for transits in the PDC-SAP data, applying a matched filter to compensate for stellar variability. TPS identified several "threshold crossing events," or possible transiting planet signals (TCEs), in the light curves of both DS Tuc A and B. Upon visual inspection of results from the initial run of TPS, our team of vetters concluded that while the periodicities detected by TPS did not corresponded to transiting planets, some of the TCEs appeared transit-like. We identified two candidate transits 8.1 days apart; a third happened to fall during the three-day period of time when *TESS* lost fine guiding. We alerted the community to the detection via the MIT *TESS* Alerts webpage[29] under the designation TOI-200. We note that the alert was issued in early November based on the first TPS run from late August. The second, archival TPS run from mid-September, which was not included in the alert, detected a TCE that corresponds to DS Tuc Ab and that passed all diagnostic tests in the data validation (DV) report.

2.1.2. Spitzer

Based on the *TESS* alert, we scheduled observations of two transits with the *Spitzer Space Telescope*, which were conducted on 2019 March 1 and 9 UTC (Program ID: 14011, PI: Newton). We observed at 4.5 μm (channel 2) using the Infrared Array Camera (IRAC; Fazio et al. 2004). We used the 32 × 32 pixel subarray, and due to the brightness of DS Tuc A, we used 0.4 s frame times. We followed the suggestions of Ingalls et al. (2012, 2016), placing DS Tuc A in the "sweet spot" of the detector and using the "peak-up" pointing mode to keep the position of the star fixed to within a half-pixel. Each transit observation consisted of a 30 minute dither, a 7.5 hr stare including the full transit, and a final 10 minute dither. Both DS Tuc A and B are present in the *Spitzer* images. In the post-cryogenic mission, IRAC has a pixel scale of 1.″2/pixel and an FWHM of 2.″0, so the binary components are resolved but not well separated (4.5 pixels).

To address the potential for flux dilution, we modeled the point spread functions (PSFs) of both components. We generated IRAC PSFs using the `prf_realize` routine as implemented in the software package `IRACSIM`[30] (Ingalls et al. 2016) and incorporated them into the PSF-fitting framework described by Martinez & Kraus (2019), modified for use with subarray images. To briefly summarize, we fit a two-source PSF model in each subarray image by performing an Markov Chain Monte Carlo (MCMC) analysis using a standard Metropolis–Hastings algorithm with Gibbs sampling. The PSF model is described by seven parameters: x-pixel coordinate of the primary centroid (x), y-pixel coordinate of the

[29] https://tess.mit.edu/alerts/

[30] https://github.com/ingalls91104/IRACSIM

primary centroid (y), image background (b), primary peak pixel value (n), projected separation (ρ), position angle (PA), and contrast (Δm). We ran four MCMC chains with 140,000 steps each, discarding the first 10% of each chain (the "burn-in" phase). Using the weighted average of the median (x, y)-centroid, ρ, PA, and Δm generated by our MCMC fits, we made a single PSF model template of DS Tuc B. This method yielded an estimate for pixel-by-pixel flux contamination levels, which we use to select the best aperture. Based on this, we selected a fixed aperture of 4×4 pixels, which minimized the level of contamination flux from DS Tuc B (2.2%), while capturing >90% of the flux from DS Tuc A.

Due to *Spitzer*'s large intra-pixel-sensitivity variations and its pointing jitter, the measured flux of the target can vary with time as the location of the star shifts on the detector (Ingalls et al. 2012). To correct for this, we used a high-resolution pixel-sensitivity variation map (PMAP; Ingalls et al. 2012), following the recommendations from the IRAC website[31] to calculate DS Tuc A's centroid position and total flux in each image within the aperture given above. We then used the `iracpc_pmap_corr` routine to calculate corrected flux values. Further details about the photometric gain map are discussed by Ingalls et al. (2012).

2.1.3. WASP

DS Tuc was observed by the WASP-South station of the Wide Angle Search for Planets (WASP; Pollacco et al. 2006) located in Sutherland, South Africa. WASP-South consists of eight cameras on an equatorial mount, each with a 2048×2048 charge-coupled device (CCD). Observations in 2010 and 2011 used 200 mm, $f/1.8$ lenses with a broadband filter spanning 400–700 nm and a plate scale of $13\farcs7$/pixel. Observations from 2012 to 2014 used 85 mm, $f/1.2$ lenses with a Sloan r' filter and a plate scale of $32''$/pixel.

Approximately 74,000 observations of the DS Tuc system were obtained over 900 nights spanning five years. DS Tuc A and B are not resolved in the WASP data, and the precision is not sufficient to detect the transit of DS Tuc Ab; these data are used to investigate the stellar rotation period (Section 3.4).

2.2. Spectroscopy

2.2.1. Southern Astrophysical Research (SOAR)/Goodman

On 2018 December 23 we acquired moderate-resolution spectra of both DS Tuc A and DS Tuc B using the Goodman High Throughput Spectrograph (Clemens et al. 2004) at the 4.1 m SOAR Telescope located at Cerro Pachón, Chile. We observed both targets at low airmass ($\sec(z) \simeq 1.4$) with clear sky conditions using the $0\farcs46$-long slit, 400 lines/mm grating and M2 setup. This yielded moderate-resolution ($R \simeq 1850$) spectra spanning 5000–9000 Å.

After basic image reduction including bias and dark subtraction, and flat-fielding, we removed sky lines in the 2D image using the chip regions adjacent to the science spectrum in the spatial direction and cosmic rays by median stacking over five images of each target. We then optimally extracted the spectrum (Horne 1986) and applied a wavelength solution derived from HgAr lamp exposures taken just before the target observations. Lastly, we flux calibrated each spectrum using spectrophotometric standards taken during the night. These data are used to determine the stellar parameters (Section 3.1).

2.2.2. Archival Data from HARPS, UVES, and FEROS

We gathered processed archival spectra from HARPS, UVES, and FEROS using the ESO archive. While the FEROS spectrum is labeled as DS Tuc B in the ESO archive, the spectral features (in particular, the strength of Hα and Hβ) clearly reveals that this spectrum belongs to DS Tuc A. These data are used in our RV analysis (Section 3.2).

2.2.3. South African Extremely Large Telescope (SALT)/High Resolution Spectrograph (HRS)

We observed independent spectra of DS Tuc A and DS Tuc B using HRS (Crause et al. 2014) on SALT (Buckley et al. 2006). We obtained spectra on the nights of 2018 November 16, 18, 19, and 21. We used the high-resolution mode, and spectra were reduced using the MIDAS pipeline (Kniazev et al. 2016, 2017).[32] The pipeline performed flat-fielding and wavelength calibration using ThAr and Ar lamps; we did not use the sky-subtracted or merged data. The nominal spectral resolutions of the blue and red arms are 65,000 and 74,000, respectively; however, the resolution achieved by the MIDAS pipeline is approximately 46,000 as a result of not accounting for the tilt of the spectral lines. These data are used in our RV analysis (Section 3.2).

2.2.4. Network of Robotic Echelle Spectrographs (NRES)/Las Cumbres Observatory's (LCO)

We observed one spectrum of DS Tuc A using LCO (Brown et al. 2013) NRES (Siverd et al. 2018) on UT 2018 December 11. Data were reduced automatically by the LCO NRES pipeline version 0.8,[33] which included basic bias/dark corrections, optimal extraction of the 1D spectrum, and wavelength calibration with ThAr lamps. The NRES pipeline also yielded a RV estimate, but we used our own determination for consistency with other analyses (see Section 3.2). The final reduced spectra have a resolution of approximately $R \simeq 53{,}000$ and cover 3800–8600 Å. The spectrum had a signal-to-noise ratio (S/N) > 50 per resolving element around the Mg b lines (≃5160 Å). These data are used in our RV analysis (Section 3.2).

2.3. High-contrast Imaging

We performed H-band integral field spectroscopy of both stars using the Gemini Planet Imager (GPI; Macintosh et al. 2014). As part of the GPI Exoplanet Survey (GPIES), DS Tuc B was observed on 2016 November 18 (program code GS-2015B-Q-500) and DS Tuc A was observed on 2016 October 22 (GS-2015B-Q500) under poor conditions, aborted after nine images, and then observed again under better conditions on 2016 November 18 (GS-2015B-Q-500). A high-order adaptive optics (AO) system compensated for atmospheric turbulence, and an apodized Lyot coronagraph was used to suppress starlight. Using 59.6 s integration times, we obtained 37.78 minutes of data with $14\fdg9$ of parallactic angle rotation for DS Tuc B and 4.97 minutes and 35.79 minutes of data with

[31] https://irachpp.spitzer.caltech.edu/page/contrib

[32] http://www.saao.ac.za/~akniazev/pub/HRS_MIDAS/HRS_pipeline.pdf

[33] https://github.com/LCOGT/nres-pipe

5°.0 and 15°.2 of parallactic angle rotation for the two observations of DS Tuc A. All three data sets were reduced using the GPIES automated data reduction pipeline (Wang et al. 2018). Briefly, the data were dark subtracted, a bad-pixel correction was applied, the microspectra positions determined using an Argon arc lamp snapshot taken right before each sequence, 3D spectral data cubes were extracted using wavelength solutions derived from deep Argon arc lamp data, the images were distortion corrected, and fiducial diffraction spots (satellite spots) were used to locate the position of the star in each image. The stellar PSF was then subtracted from each image using both angular differential imaging (Marois et al. 2006) and spectral differential imaging (Sparks & Ford 2002) to disentangle the stellar PSF from any potential companions, and principal component analysis to model the stellar PSF (Soummer et al. 2012; Wang et al. 2015). The resulting image was then used to search for point sources (Section 4.2).

2.4. Literature Photometry and Astrometry

To better characterize the properties of each component we drew resolved photometry and astrometry for DS Tuc A and DS Tuc B from the literature. Specifically, we adopted optical B_T and V_T photometry from the Tycho-2 Survey (Høg et al. 2000), optical G, BP, and RP photometry from the *Gaia* second data release (DR2; Evans et al. 2018), near-infrared J, H, and K_S photometry from The Two Micron All Sky Survey (2MASS; Skrutskie et al. 2006), and mid-infrared $W1$, $W2$, $W3$, and $W4$ photometry from the *Wide-field Infrared Survey Explorer* (*WISE*; Wright et al. 2010). We also adopted proper motions and parallaxes for each component from DR2 (Lindegren et al. 2018), and J2000 positions from Tycho-2.

All photometry and astrometry from the literature used in our analysis is listed in Table 1.

3. Measurements

3.1. Stellar Parameters

Age: DS Tuc was one of the original systems used to define the Tuc-Hor moving group (then called the Tucanae association; Zuckerman & Webb 2000). The group has consistent age estimates based on isochronal fitting (45 ± 4 Myr; Bell et al. 2015) and the lithium-depletion boundary (40 Myr; Kraus et al. 2014). Here we adopt the age estimate from Bell et al. (2015).

Luminosity, effective temperature, and Radius: We first determined the bolometric flux ($F_{\rm bol}$), $T_{\rm eff}$, and angular diameter of DS Tuc A and DS Tuc B by fitting the resolved spectral energy distributions (SEDs) for each component with unreddened optical and near-infrared template spectra from the cool stars library (Rayner et al. 2009). A demonstration can be seen in Figure 2.

Our SED-fitting procedure followed the technique outlined in Mann et al. (2015), which we briefly summarize here. Our comparison assumed zero reddening, as DS Tuc lands within a region near the Sun of low interstellar extinction (the Local Bubble; Sfeir et al. 1999). We simultaneously compared each template spectrum to our optical spectra from SOAR/Goodman (Section 2.2.1) and archival photometry (Section 2.4 and Table 1) using the appropriate system zero-point and filter profile (Cohen et al. 2003; Jarrett et al. 2011; Mann & von Braun 2015; Maíz Apellániz & Weiler 2018). Gaps in each template spectrum are filled with a BT-SETTL atmospheric model (Allard et al. 2012) using the model interpolation and fitting procedure described in Gaidos et al. (2014). This procedure simultaneously provided an estimate of $T_{\rm eff}$ based on the BT-SETTL model comparison to the observed spectrum. To compute $F_{\rm bol}$, we integrated each template/model combination over all wavelengths.

We combined the derived $F_{\rm bol}$ with the *Gaia* DR2 distance (d) to determine the total luminosity (L_*) for each component star. We then calculated a stellar radius (R_*) from L_* and $T_{\rm eff}$ using the Stefan–Boltzmann relation. Errors on each parameter were assigned accounting for both the measurement uncertainties (e.g., in the photometry) as well as the range of possible templates (and their assigned $T_{\rm eff}$ values) that can fit the data. Final parameters and uncertainties are give in Table 1.

As part of our above procedure, the BT-SETTL model is scaled to match the photometry and template. Assuming perfect models, this multiplicative scale factor is equal to R_*^2/d^2 (Cushing et al. 2008), which provided another estimate of R_* given the *Gaia* DR2 distance. This technique is similar to the infrared-flux method (Blackwell & Shallis 1977). Radii derived from this scale factor are not totally independent of the above method, as they rely on the same photometry and models, but the latter technique is less sensitive to the assigned $T_{\rm eff}$.

The first technique (Stefan–Boltzman) yielded a radius of $0.964 \pm 0.029 R_\odot$, and the scaling (infrared-flux method) yielded a consistent radius of $0.951 \pm 0.020 R_\odot$ for DS Tuc A. We adopt the former value for all analyses.

Mass: We estimated the masses of DS Tuc A and DS Tuc B by interpolating our luminosity estimates onto a modified isochrone grid from the Dartmouth Stellar Evolution Program (Dotter et al. 2008). These grids were adjusted to include the effects of magnetic fields and where the boundary conditions are applied, as described in more detail in Muirhead et al. (2014), Feiden & Chaboyer (2014), and Feiden (2016). We assumed solar metallicity, which is typical within a scatter of ~0.1 dex for the young stellar populations in the Solar neighborhood (e.g., Spina et al. 2014 and references therein). We used both 40 and 50 Myr grids, using the spread to approximate errors introduced by the age uncertainty for the Tuc-Hor moving group. This interpolation yielded mass estimates of $1.01 \pm 0.06 M_\odot$ for DS Tuc A and $0.84 \pm 0.06 M_\odot$ for DS Tuc B. We considered these errors to be slightly underestimated, as systematic differences between model grids can exceed 10% at this age.

3.2. RVs

We used high-resolution data from HARPS, UVES, FEROS, SALT/HRS, and NRES/LCO to determine stellar RVs. We measured RVs by computing the spectral line broadening function (BF; Rucinski 1992) between DS Tuc A or B observations and a zero-velocity template. The BF represents the function that, when convolved with the template, returns the observed spectrum, carrying information on RV shifts and line broadening. Throughout the analysis we used the HARPS G2 binary mask as our template (e.g., Pepe et al. 2002). A Gaussian profile was fit to the BF to determine the stellar RV. In each case the BF is single peaked and smooth, indicating a contribution from only one star.

For each echelle order we computed a "first pass" BF, which was used to shift the observed spectrum near zero velocity. Orders that survive a 3σ-clipping algorithm were then stitched into three equal-length wavelength regions where the final BFs were computed. Our geocentric RV measurement and uncertainty were computed from the mean and standard deviation across these three regions. For archival observations that are

Table 1
Parameters of DS Tuc

Parameter	DS Tuc A	DS Tuc B	Source
	Identifiers		
TOI	200.01		
Gaia DR2	6387058411482257536	6387058411482257280	*Gaia* DR2
TIC	410214986	410214984	Stassun et al. (2018)
2MASS	J23393949-6911448	J23393929-6911396	2MASS
HD	222259A	222259B	Cannon & Pickering (1924)
	Astrometry		
α R.A. (hh:mm:ss J2000)	23:39:39.49	23:39:39.27	Tycho-2
δ decl. (dd:mm:ss J2000)	−69:11:44.88	−69:11:39.51	Tycho-2
μ_α (mas yr^{-1})	79.464 ± 0.074	78.022 ± 0.064	*Gaia* DR2
$\mu\delta$ (mas yr^{-1})	−67.440 ± 0.045	−65.746 ± 0.037	*Gaia* DR2
π (mas)	22.666 ± 0.035	22.650 ± 0.030	*Gaia* DR2
	Photometry		
B_T (mag)	9.320 ± 0.017	10.921 ± 0.060	Tycho-2
V_T (mag)	8.548 ± 0.012	9.653 ± 0.030	Tycho-2
G (mag)	8.3193 ± 0.0010	9.3993 ± 0.0014	*Gaia* DR2
G_{BP} (mag)	8.7044 ± 0.0049	9.9851 ± 0.0059	*Gaia* DR2
G_{RP} (mag)	7.8137 ± 0.0036	8.7082 ± 0.0044	*Gaia* DR2
J (mag)	7.122 ± 0.024	7.630 ± 0.058	2MASS
H (mag)	6.759 ± 0.023	7.193 ± 0.034	2MASS
K_s (mag)	6.68 ± 0.03	7.032 ± 0.063	2MASS
$W1$ (mag)	6.844 ± 0.060	7.049 ± 0.081	*WISE*
$W2$ (mag)	6.748 ± 0.030	7.107 ± 0.037	*WISE*
$W3$ (mag)	6.777 ± 0.023	7.056 ± 0.029	*WISE*
$W4$ (mag)	6.668 ± 0.094	6.958 ± 0.119	*WISE*
	Kinematics		
Barycentric RV (km s^{-1})	8.05 ± 0.06	6.41 ± 0.06	This work
U (km s^{-1})	−8.71 ± 0.04	−9.27 ± 0.04	This work
V (km s^{-1})	−21.50 ± 0.04	−20.28 ± 0.04	This work
W (km s^{-1})	−1.53 ± 0.04	−0.47 ± 0.04	This work
	Physical Properties		
Spectral type	G6V ± 1	K3V ± 1	Torres et al. (2006)
Rotation period (days)	$2.85^{+0.04}_{-0.05}$	unknown	This work
$T_{\rm eff}$ (K)	5428 ± 80	4700 ± 90	This work
$F_{\rm bol}$ (10^{-8} erg cm^{-2} s^{-1})	1.2026 ± 0.017	0.542 ± 0.008	This work
M_* ($M_\odot$)	1.01 ± 0.06	0.84 ± 0.06	This work
R_* ($R_\odot$)	0.964 ± 0.029	0.864 ± 0.036	This work
L_* ($L_\odot$)	0.725 ± 0.013	0.327 ± 0.010	This work
Age (Myr)	45 ± 4	45 ± 4	Bell et al. (2015)
$v \sin i_*$ (km s^{-1})	17.8 ± 0.2	14.4 ± 0.3	This work
i_* (deg)[a]	>82°	...	This work

Note.
[a] With the convention $i < 90$.

provided as a single stitched spectrum, we created 150 Å wide initial "orders."

Finally, for each epoch we computed the BF for telluric absorption features using a continuum normalized A0 star as our template. These offsets were applied to our measured RVs. We have measured RVs for all archival data following the above procedure. While the HARPS pipeline provides more precise RVs, we preformed our own measurements to ensure the same zero-point corrections across different instruments. We found a ∼70 m s^{-1} offset from the HARPS observations, similar to our measurement uncertainty, but recovered the same epoch-to-epoch variability. Our final RVs are corrected for barycentric motion and listed in Table 2. As noted in the introduction, DS Tuc B was previously identified as a binary based on its RV variability and the presence of two spectral components. Our spectra are inconsistent with DS Tuc B having two near-equal spectral type components; for both stars at each epoch, there is only one peak in the BF. While the previous work did not give sufficient information to test the proposed scenario of RV variability, we also do not see evidence for RV variations in excess of reasonable jitter levels for young stars in either star.

3.3. Projected Rotation Velocity

We measured the projected rotation velocity ($v \sin i_*$) for DS Tuc A and B by fitting the BF with a rotationally broadened absorption line profile that has been convolved with the

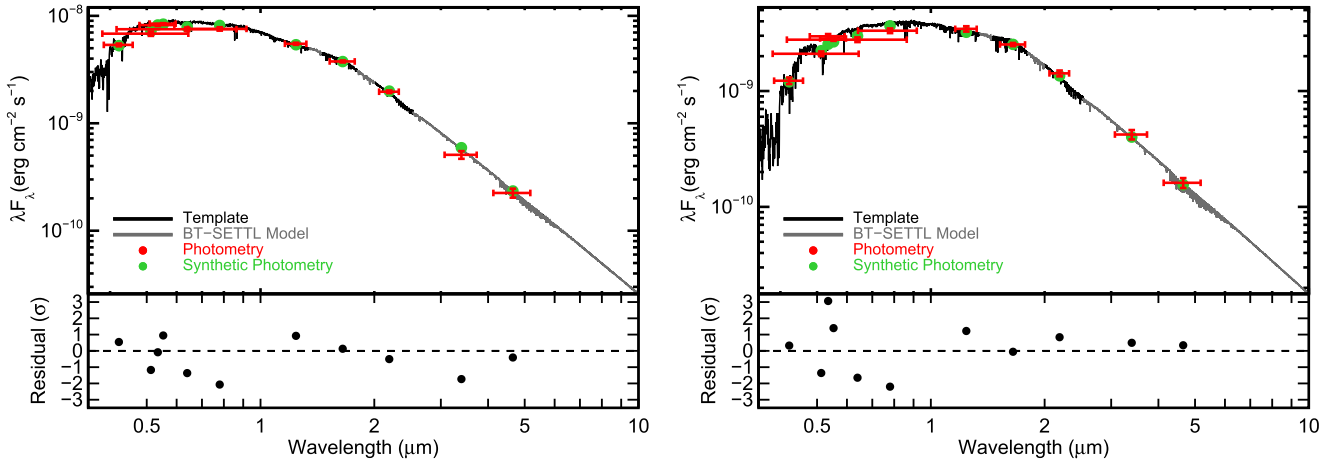

Figure 2. Best-fit spectral template compared to the photometry of DS Tuc A (left) and DS Tuc B (right). Gray regions are BT-SETTL models, used to fill in gaps or regions of high telluric contamination. Literature photometry is shown in red, with horizontal errors corresponding to the filter width and vertical errors the measurement errors. Corresponding synthetic photometry is shown as green points. The bottom panel shows the residuals in terms of standard deviations from the fit.

Table 2
RV Measurements of DS Tuc A and B

Site	BJD	RV (km s^{-1})	σ_{RV} (km s^{-1})
	DS Tuc A		
HARPS	2453500.876233	7.82	0.07
HARPS	2453521.828166	7.93	0.05
HARPS	2453522.888133	8.32	0.06
HARPS	2453541.927465	8.02	0.07
HARPS	2453600.704290	7.85	0.07
UVES	2454243.856154	8.27	0.10
FEROS	2455853.592265	7.98	0.24
SALT	2458439.283495	8.08	0.43
SALT	2458441.278033	8.29	0.46
SALT	2458442.295852	8.34	0.28
SALT	2458444.297823	7.74	0.31
LCO	2458463.540450	8.28	0.15
Mean: 8.05 (km s^{-1})			
rms: 0.21 (km s^{-1})			
Std. Error: 0.06 (km s^{-1})			
	DS Tuc B		
SALT	2458439.288665	6.41	0.31
SALT	2458441.273940	6.66	0.30
SALT	2458442.302087	6.42	0.21
SALT	2458444.302819	6.33	0.27
UVES	2454243.850252	6.25	0.11
Mean: 6.41 (km s^{-1})			
rms: 0.14 (km s^{-1})			
Std Error: 0.06 (km s^{-1})			

instrumental profile (Figure 3). We did not include additional broadening components such as microturbulence, though these factors should have minimal impact given the large $v \sin i_*$ values. For DS Tuc A, we find $v \sin i_* = 17.8 \pm 0.2$ km s^{-1} using the HARPS spectra; the value is consistent when using SALT/HRS. From SALT/HRS observations of DS Tuc B, we measure $v \sin i_* = 14.4 \pm 0.3$ km s^{-1}.

3.4. Stellar Rotation

Rotation period: A photometric rotation period of 2.85 days for DS Tuc was previously reported by Kiraga (2012), and is

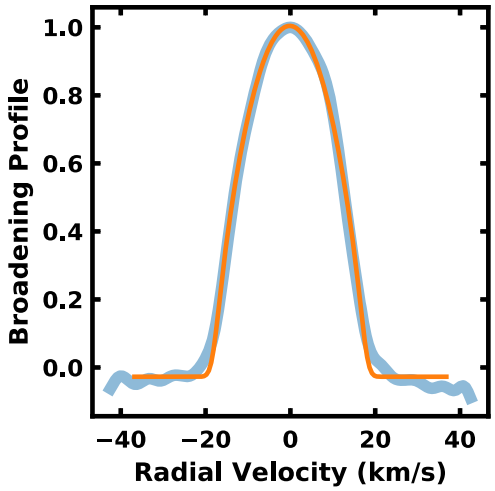

Figure 3. DS Tuc A broadening function computed from a representative HARPS spectrum. The broadening function presented in blue is clearly single peaked and rotationally broadened. A best-fit rotational broadening profile is over plotted in orange. Extended wings in the broadening function as compared to the rotational broadening profile arise from additional line broadening mechanisms (macro/microturbulence), which are not included in our pure-rotation model.

clearly visible in both the *TESS* and WASP light curves. Using ground-based monitoring with the LCO, we associate this signal with DS Tuc A. We break the WASP light curve into four 200 day observing seasons and measure the rotation period and amplitude of variability in each season. The period is consistently 2.85 days with high variability in the semi-amplitude (2%–2.6%), but the phase shifts. The periodogram shows power at the period and the first harmonic, and no additional signals are seen that could be associated with DS Tuc B.

The *TESS* light curve of DS Tuc shows consistent rotational modulation with a semi-amplitude of 1%–2%. We modeled the *TESS* light curve with a Gaussian process (GP) using the `celerite` package from Foreman-Mackey et al. (2017). We used a kernel composed of a mixture of simple harmonic oscillators and a jitter term. Our GP model has a term to capture the periodic brightness modulation caused by spots on the stellar surface. This kernel is a mixture of two stochastically

Table 3
Stellar Binary Orbital Parameters

Element	Median	Std. Dev.	Mode	68.3% Min. CI	95.4% Min. CI
a (au)	176	29	160	(157, 174)	(157, 219)
P (yr)	1760	510	1500	(1470,1730)	(1470,2440)
e	0.57	0.10	0.47	(0.46, 0.60)	(0.46, 0.77)
i (°)	96.9	0.9	96.6	(96.0, 97.8)	(95.0, 98.6)
ω (°)	186	35	196	(164, 233)	(122, 256)
Ω (°)	−12	3	−13	(−15, −10)	(−18, −6)
T_0 (yr)	1250	480	1520	(1250, 1530)	(−590, 1530)
Periastron (au)	75	17	85	(59, 93)	(44, 105)

Note. We report the median, mode, standard deviation, and 68.3% and 95.4% minimum credible intervals, with marginal posteriors and joint distributions displayed in Figure 4.

driven, damped harmonic oscillator models and has two modes in Fourier space: one at the rotation period of the star and one at half the rotation period. We initially included an additional damped harmonic oscillator with a period of 20 days to capture long-term trends in the light curve, but the fitted power of the signal indicated that it was unnecessary.

We used a Lomb–Scargle periodogram to identify the candidate rotation period. We then fit the stellar rotation model using least squares, iterating five times and rejecting 3σ outliers each pass. This served to remove smaller flares. We then started an MCMC fit using the affine-invariant MCMC implemented in the package `emcee` (Foreman-Mackey et al. 2013), beginning half the chains at the candidate rotation period identified in the periodogram, and a quarter each at half and twice the rotation period. We use 50 walkers and a burn-in of 5000 steps. We end the run when the autocorrelation timescale τ of all chains changes by <0.1 and the length of the chain is $>100\tau$. We measure a rotation period of $2.85^{+0.04}_{-0.05}$ days.

Stellar inclination: Following the method detailed in Morton & Winn (2014), we combined the stellar rotation period measured from the *TESS* light curve, R_*, and $v \sin i_*$ measurements from above to estimate of the stellar inclination for DS Tuc A. Although this measurement is not very precise, this method can identify highly misaligned systems (e.g., Hirano et al. 2012) or be used for statistical studies of large planet populations (e.g., Winn et al. 2017). We determine an equatorial velocity of $17.13 \pm 0.6\,\mathrm{km\,s^{-1}}$, which is consistent with our spectroscopic measurement of $v \sin i_* = 17.8 \pm 0.2\ \mathrm{km\,s^{-1}}$. This corresponds to a 1σ lower limit on the inclination of $i > 82°$ and a 2σ lower limit of $i > 70°$. We cannot distinguish between $i < 90°$ and $i > 90°$, and so adopt the convention $i < 90°$.

4. Constraints on the DS Tuc System Architecture

4.1. Stellar Binary Orbit

We fit orbital parameters to the motion of the binary pair using a modified implementation of the Orbits for the Impatient (OFTI) rejection-sampling methodology described in Blunt et al. (2017). This implementation is publicly available on GitHub[34] and described further in Pearce et al. (2019).

Both objects have a well-defined *Gaia* DR2 astrometric solution, so we used the positions and proper motions of DS Tuc B relative to DS Tuc A in the plane of the sky. We used the RV measurements of Table 2 to interpolate a relative RV at the *Gaia* observation epoch of 2015.5. Relative separation and position angle (PA) measurements in the Washington Double Star Catalog (WDS) spanning 126 yr provide additional constraints on the stellar orbital motion. We performed a modified OFTI fit constrained by these measurements.

Previous implementations of OFTI have fit orbital parameters to astrometric observations spanning several epochs (e.g., Blunt et al. 2017; Cheetham et al. 2019; Pearce et al. 2019; Ruane et al. 2019). In this system, the precision of the *Gaia* solution for both objects allowed us to constrain five of the six position vector elements using just this single epoch, and we additionally have the astrometric measurements provided by WDS; only the line of sight position is not sufficiently constrained to contribute to the fit.

Table 3 displays the orbital parameters we determined for the stellar binary orbit. Figure 4 displays the orbital parameter distributions, joint credible intervals, and a selection of orbits plotted in the plane of the sky. The orbital semimajor axis is $157 < a < 174$ au, with a closest approach of $59 < r_{\mathrm{peri}} < 93$ au (where the ranges are 1σ credible intervals). The stellar binary is constrained to be nearly edge-on ($96.^{\circ}0 < i < 97.^{\circ}8$), which is likely aligned with both the transiting planet's orbit and the primary star's spin axis.

4.2. Limits on Additional Directly Imaged Companions

To search for companions in high-contrast imaging data from GPI, we forward modeled the PSF template of a hypothetical companion at each pixel in the image using the Forward Model Matched Filter technique (FMMF; Ruffio et al. 2017a). We then ran a matched filter with the template in an attempt to maximize the signal of a planet at that location in the image. The method accounts for the distortion of the signal due to the speckle subtraction step. The detection limits are expressed in terms of the flux ratio between the point source and the star and were calibrated using simulated point-source injection and recovery. The detection limits are set at six times the standard deviation of the noise in the final image, which is calculated in concentric annuli as a function of separation to the star. This detection threshold ensures a false-positive rate of less than one per 20 sequence of observations. The default matched filter reduction used for GPIES assumes a featureless spectrum, corresponding to hot planets, for the estimation of the point-source brightness. However, Ruffio et al. (2017b) showed that it can be used for the detection of stars without loss of sensitivity. We did not detect any candidate companions above our detection threshold in either data set.

We determined completeness to bound substellar companions using the method described in Nielsen et al. (2019). An ensemble of simulated companions were generated with full

[34] https://github.com/logan-pearce/LOFTI (Pearce 2019).

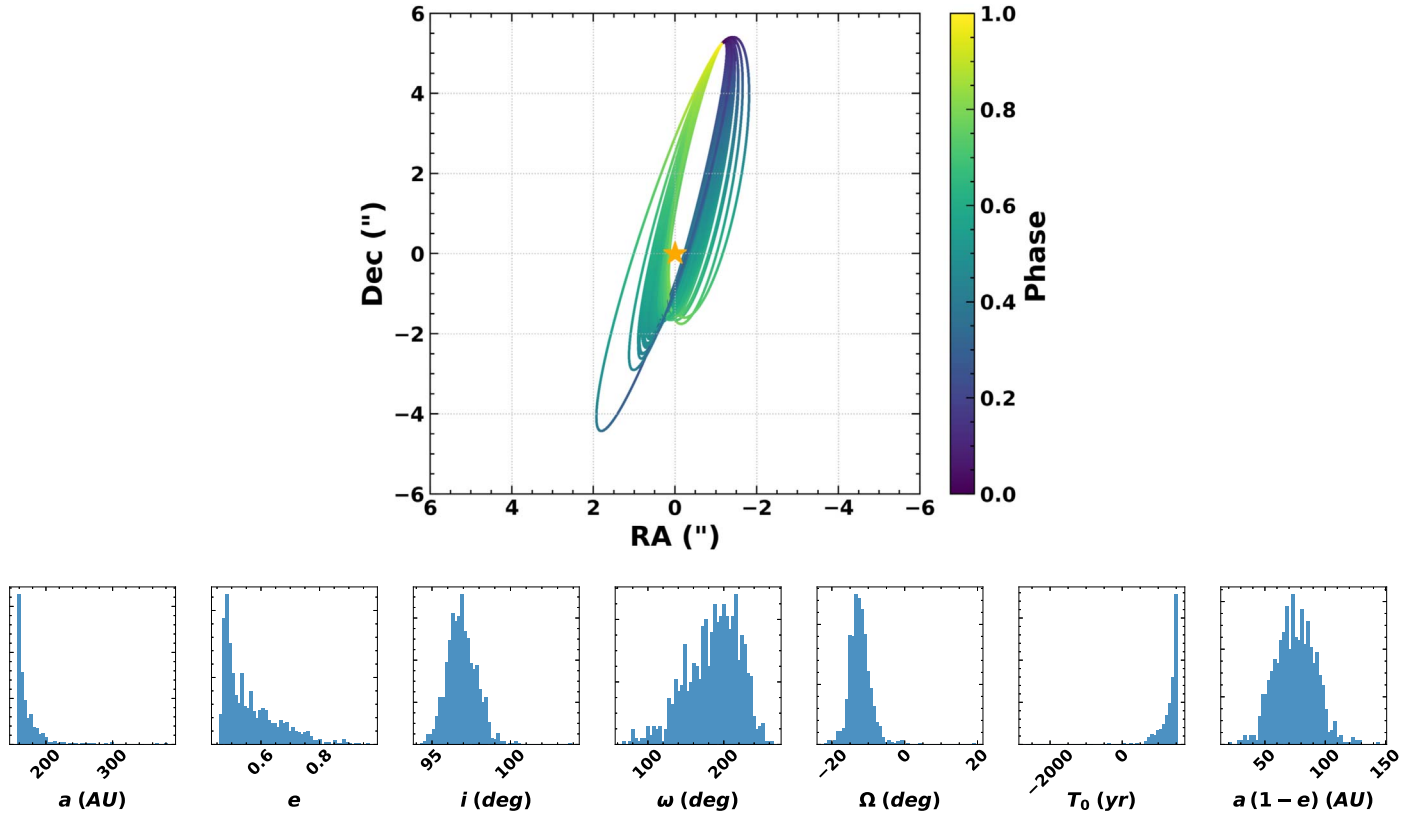

Figure 4. Top panels: 100 randomly selected orbits from the posterior distribution of accepted orbits for the stellar binary system. DS Tuc A is marked by the orange star at the origin, while the present position of DS Tuc B relative to A is located where the orbit tracks converge. Orbital phase is shown by the color bar, with an orbital phase of 0.0 corresponding to the *Gaia* observation epoch 2015.5. Bottom panels: posterior distributions for all orbital parameters from the fit, as well as periastron. Semimajor axis and epoch of periastron passage have been truncated for clarity. The inclination is tightly constrained to be nearly edge-on (90°), close to the inclination of the transiting planet.

orbital parameters at a grid of semimajor axis and planet mass. The projected separation in arcseconds was then computed for each simulated companion given the distance to the star, and the contrast was calculated using the BT-Settl models (Baraffe et al. 2015), the age of the star (45 Myr), and the star's H magnitude. Each simulated companion was compared to the measured contrast curve, and companions lying above the curve were considered detectable. The same simulated companions were compared to multiple contrast curves, advanced forward in their orbits when observations are made at different epochs, as is the case for DS Tuc A. Outside a radius of $\sim 1\farcs1$, not all PAs fall on the detector; to compensate, we reduce the completeness beyond $\sim 1\farcs1$ using the fractional coverage as a function of radius.

The depth of search plots, giving completeness as a function of semimajor axis and companion mass, are given for DS Tuc A and B in Figure 5, along with the underlying contrast curves. There are two contrast curves at each epoch: a T-type curve assuming heavy methane absorption in the matched filter step (appropriate to companions as hot as ∼1100 K), and an L type contrast curve assuming a flatter spectrum appropriate to hotter brown dwarfs and stars. Overall, wider separation planets and brown dwarfs are ruled out at high confidence between ∼10–80 au, more massive than ∼5 $M_{\rm Jup}$, around both A and B.

4.3. Limits on Wide Binary Companions

Past AO observations of the DS Tuc system have been limited to an outer working angle of $\rho \lesssim 10''$ (e.g., Kasper et al. 2007), leaving open the possibility of a hierarchical architecture with a very wide tertiary companion. The Gaia catalog reveals that there is one co-moving, codistant candidate Tuc-Hor member within <1 pc of the DS Tuc system, 2MASS J23321028-6926537, which was also suggested to be a candidate low-mass (spectral type around M5) member of Tuc-Hor by Gagné et al. (2015). However, given the very wide separation ($\rho = 1.12 \times 10^5$ au), this source is likely an unbound member of Tuc-Hor and not a bound companion of DS Tuc. There are no other candidate wide companions in *Gaia* DR2 within $\rho < 1$ pc and brighter than a limiting magnitude of $G \sim 20.5$ mag, corresponding to a mass limit of $M > 15 M_{\rm Jup}$ at $\tau = 40$ Myr (Baraffe et al. 2015).

4.4. Limits on Additional Transiting Planets

We tested the detectability of additional planets in the *TESS* sector 1 light curve of DS Tuc A using the notch-filter detrending and planet search pipeline of Rizzuto et al. (2017). For this process, we used the SAP light curve, which is not corrected for systematics using the cotrending basis vector method. This choice was made based on the presence of artifacts in the PDCSAP light curve, likely introduced by the presence of a strong stellar rotation signal. We first apply a deblending factor based on the *TESS* magnitudes for DS Tuc A and B and masked the time interval when fine guiding was lost. We then injected a set of model transiting planets synthesized with the BATMAN model of Kreidberg (2015) with orbital and size parameters chosen randomly. We used orbital periods of 1–20 days and planet radii of 1–10 $R_\oplus$, and

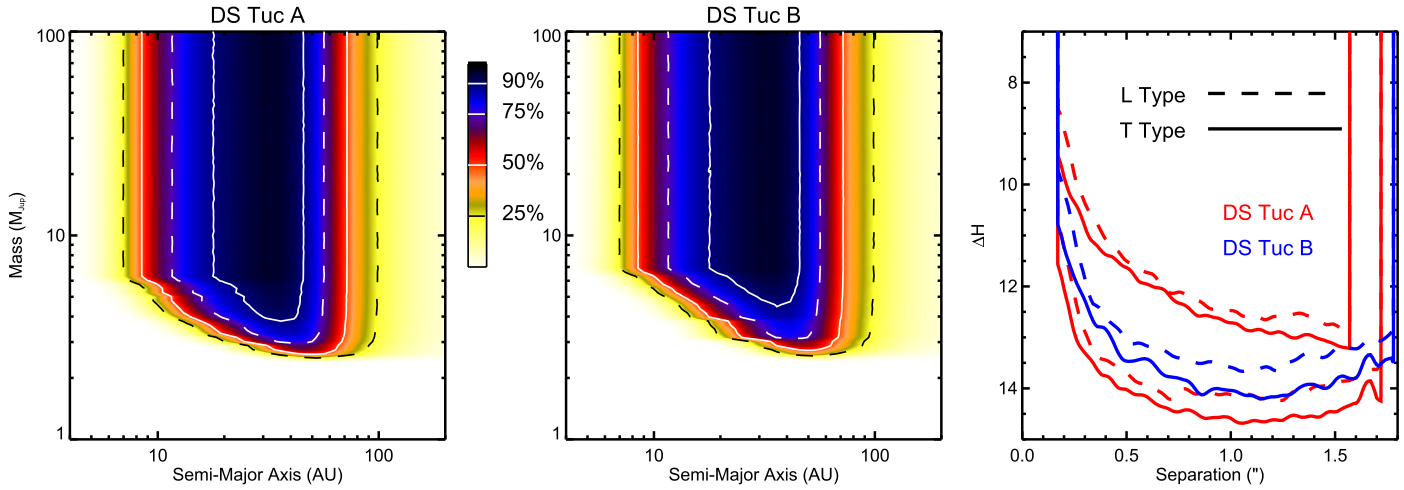

Figure 5. Left and middle panels: completeness to substellar companions from the GPIES observations of DS Tuc A and B. Planets and brown dwarfs more massive than $\sim$5 $M_{\rm Jup}$ are excluded at high completeness between 10 and 80 au. Right panel: contrast curves from which these completeness maps are derived, based on two epochs of GPIES observations of DS Tuc A, and one of B. The contrast limits are slightly deeper for T-type spectra, as PSF subtraction can leverage the strong methane absorption for the coolest planets.

allowed orbital phase and impact parameter to take values in the interval [0,1]. Eccentricity was fixed to zero for this process, as it does not significantly influence detectability of a transit, but requires two additional variables over which to marginalize. We injected a total of 1000 trial planets for this test.

For each trial planet, we apply the notch-filter detrending pipeline, and then search for periodic signals with the BLS algorithm (Kovács et al. 2002), retaining signals with power-spectrum peaks above 7σ. We then set tolerance windows of 1% in both injected period and orbital phase to flag a trial planet as recovered. Figure 6 shows the completeness map for additional planets in the DS Tuc A system. Our search and the *TESS* sector 1 data for DS Tuc A are sensitive to $\sim 4\,R_\oplus$ planets at period $<$10 days, and $\sim 3\,R_\oplus$ at periods $<$6 days. At periods longer than 10 days, the time baseline and gaps due to the masked section significantly decrease sensitivity to transiting planets.

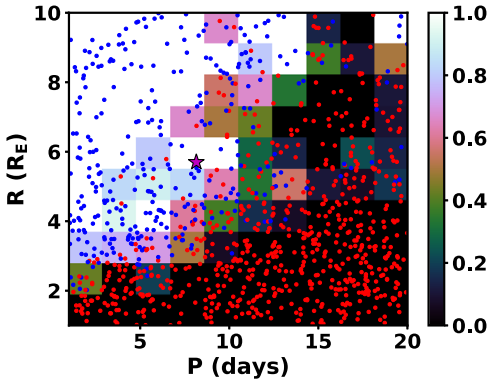

Figure 6. Completeness map for additional planets in the DS Tuc A system, produced from injection-recovery testing of our search pipeline (Rizzuto et al. 2017). Each point represents an injected planet signal, with blue points indicating recovery and red points indicating non-recovery. The magenta star marks the position of the detected planet DS Tuc Ab.

5. Analysis of the Planetary Signal

5.1. Identification of the Stellar Host

The two components of DS Tuc are separated by 5″ and are not resolved by *TESS*,[35] which has a plate scale of 21″ pixel^{-1} with 50% of light concentrated within one pixel (Ricker et al. 2014). We examined the measured centroid of the in-transit/out-of-transit difference image, which is calculated by the SPOC pipeline and included in the DV report (from the initial TPS run) that accompanied the alert. The DV report indicated that both DS Tuc A and B are contained within the 3σ confusion radius of the centroid (which we note is dominated by the 2.″5 additional error added in quadrature to the propagated uncertainty) and the centroid analysis averages a transit signal and a spurious event. In the second TPS run, not included in the alert, the centroid offset is consistent with DS Tuc A at 2σ. We also analyzed the image centroids measured by the SPOC pipeline. The scatter in the centroid measurements is too large ($\simeq$1 millipixel per 4 hr bin) to detect the expected change in centroid position if the planet were to in fact orbit DS Tuc B (0.5 millipixel over a 3 hr transit). In summary, we found that the *TESS* data alone cannot conclusively identify which star hosts the transit.

Our *Spitzer* observations definitively show that the planet orbits DS Tuc A. A 4 × 4 pixel aperture placed on DS Tuc A revealed a transit signal that is consistent with that detected in the *TESS* data. An equal-sized or smaller aperture centered on DS Tuc B yielded no detectable transit signature (Figure 7).

5.2. Transit Fitting

We simultaneously fit the *TESS* and *Spitzer* photometry using the transit fitting code `misttborn`.[36] `misttborn` was first used in Mann et al. (2016a) and has been used for a number of more recent works including Johnson et al. (2018). Briefly, we fit each system using `emcee`, and produced photometric transit models using `batman` (Kreidberg 2015), which is based on the transit model of Mandel & Agol (2002). In the MCMC we fit for the following planetary parameters: the

[35] The *TESS* alert somewhat arbitrarily identifies DS Tuc A as the host because it is the brightest star in the vicinity.

[36] https://github.com/captain-exoplanet/misttborn

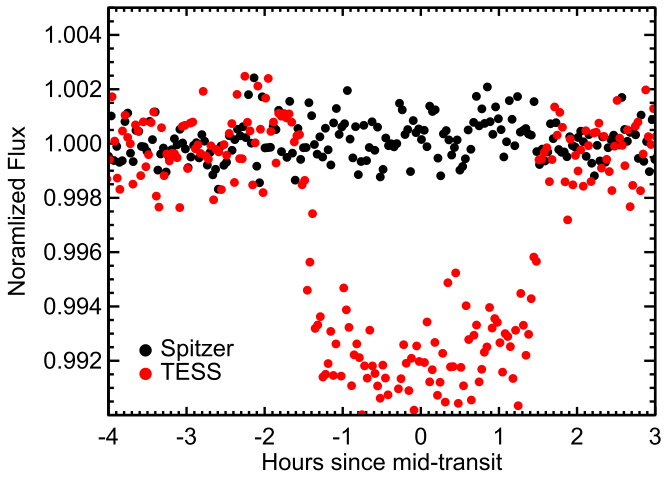

Figure 7. *Spitzer* light curve from 2019 March 1 for a 4 × 4 pixel aperture centered on DS Tuc B (black) compared to the *TESS* photometry at an aperture centered on DS Tuc B (red). The *TESS* data shown here assumes (incorrectly) that the planet orbits DS Tuc B, and it has been corrected for contamination from DS Tuc A. Flux measurements from *Spitzer* were binned with 300 measurements per bin for clarity. In the resolved *Spitzer* data, DS Tuc B shows no transit signal, and we thus conclude that the planet orbits DS Tuc A.

planet-to-star radius ratio $R_P/R_\star$ (assumed to be the same in all filters), impact parameter b, period P, and the epoch of the transit midpoint T_0. We fix eccentricity to zero. We also fit the following stellar parameters: linear and quadratic limb-darkening parameters for each filter (q_1, q_2) using the triangular sampling method of Kipping (2013), and the mean stellar density ($\rho_\star$). We use Gaussian priors for the limb-darkening parameters, using the values in Claret & Bloemen (2011) and Claret (2017). We use uniform priors within physically allowed boundaries for the remaining parameters (most notably, we enforced $|b| < 1 + R_P/R_\star$ in order to assure that a transit occurs while allowing grazing transits).

DS Tuc is a visual binary with a separation of $\rho \sim 5''$. The *TESS* photometry is de-blended, but the deblending process may introduce errors, while our *Spitzer* aperture on DS Tuc A includes a small amount of contamination from DS Tuc B. We included as an additional MCMC parameter the contamination of the aperture by flux from other stars. This is implemented as a (fractional) flux added to the transit model to create a diluted model ($\mathrm{LC_{diluted}}$) of the form

$$\mathrm{LC_{diluted}} = \frac{\mathrm{LC_{undiluted}} + C}{1 + C}, \quad (1)$$

where $\mathrm{LC_{undiluted}}$ is the model light curve generated from `Batman` and our GP model. This is comparable to the method used in Johnson et al. (2011) and Gaidos et al. (2016) to correct for flux dilution from a binary using the measured Δm between components. The key difference is that Equation (1) allows for flux to be subtracted from the model ($C < 0$) in the case of an overcorrection.

We set a Gaussian prior upon C of 0.00 ± 0.02 for *TESS* and 0.0217 ± 0.0050 for *Spitzer*. The width of 0.02 for *TESS* photometry was estimated based on uncertainties in the derived *TESS* magnitudes from the TIC. Section 2.1.2 describes how C for *Spitzer* was calculated from a model of the PSF.

The target displays substantial stellar variability in the *TESS* bandpass. In addition to the transit model described above, we utilized Gaussian process regression to account for stellar variability in the *TESS* photometry. This enables us to model the variations in the stellar flux occurring during the transit. Our kernel is a mixture of simple harmonic oscillators, the same as described in Section 3. We included the Gaussian process hyperparameters as fit parameters in our MCMC, and placed priors on those parameters based on the results of our stellar rotation modeling. The parameters are the stellar rotation period P_*, the amplitude A_{GP} of the primary signal at P_*, the relative strength of the secondary signal at $P_*/2$ ($\mathrm{Mix}_{Q1,Q2}$), the decay timescales of the primary and secondary signals ($Q1_{\mathrm{GP}}$, $Q2_{\mathrm{GP}}$), and a jitter term to account for white noise (σ_{GP}).[37]

We ran the MCMC chain with 100 walkers for 30,000 steps and cut off the first 5000 steps of burn-in, producing a total of 2.5×10^6 samples from the posterior distributions of the fit parameters. The resulting fit is shown in Figure 1, and the best-fitting values are listed in Table 4.

Table 4
Parameters of DS Tuc Ab

Parameter	Value
Measured Parameters	
T_0 (TJD)[a]	1332.30997 ± 0.00026
P (days)	$8.138268 \pm 1.1 \times 10^{-5}$
$R_P/R_\star$	0.05419 ± 0.00024
b	$0.18^{+0.13}_{-0.12}$
ρ_* ($\rho_\odot$)	$1.7^{+0.07}_{-0.17}$
$q_{1,1}$	$0.284^{+0.055}_{-0.053}$
$q_{2,1}$	0.284 ± 0.051
$q_{1,2}$	$0.0266^{+0.0094}_{-0.0091}$
$q_{2,2}$	$0.054^{+0.014}_{-0.013}$
C_{TESS}	$0.015^{+0.018}_{-0.017}$
$C_{Spitzer}$	$0.0208^{+0.0049}_{-0.005}$
$\ln P_*$ (day)	$1.0606^{+0.0102}_{-0.0098}$
$\ln A_{\mathrm{GP}}$ ($\%^2$)	$-10.87^{+0.11}_{-0.12}$
$\ln Q1_{\mathrm{GP}}$	$2.57^{+0.39}_{-0.37}$
$\ln Q2_{\mathrm{GP}}$	$0.052^{+0.027}_{-0.026}$
$\mathrm{Mix}_{Q1,\ Q2}$	$0.15^{+0.26}_{-0.11}$
σ_{GP}	-8.682 ± 0.013
Derived Parameters	
$R_P(R_\oplus)$	5.70 ± 0.17
$a/R_\star$	$20.35^{+0.29}_{-0.69}$
$i(^\circ)$	$89.5^{+0.34}_{-0.41}$
δ (%)	0.2936 ± 0.0026
T_{14} (days)	$0.13235^{+0.00049}_{-0.00039}$
T_{23} (days)	$0.11818^{+0.00039}_{-0.00057}$
T_{peri} (TJD)[a]	1332.30997 ± 0.00026
$g_{1,1}$	$0.3^{+0.055}_{-0.054}$
$g_{2,1}$	$0.228^{+0.066}_{-0.06}$
$g_{1,2}$	$0.0172^{+0.0057}_{-0.0051}$
$g_{2,2}$	$0.145^{+0.024}_{-0.028}$

Notes. We report the median and 68% confidence interval for each parameter. Associated probability distributions for key parameters are shown in Figure 1.
[a] TJD is *TESS* Julian Date, which is BJD-2,457,000.0.
[b] Although we allow b to explore negative values, the absolute value of b is listed because positive and negative values are degenerate. Similarly, we cannot distinguish between $i < 90^\circ$ and $i > 90^\circ$ and adopt the convention $i < 90^\circ$.

[37] https://celerite.readthedocs.io/en/stable/python/kernel/

5.3. False-positive Analysis

As we do not have dynamical (RV) confirmation of DS Tuc Ab, we use our other observations to show that the transits are caused by a real transiting planet. We consider and rule out the following false-positive scenarios.

1. *The transits are caused by instrumental artifacts or residuals from stellar variability:* Though there are only two transits in the *TESS* data set with amplitudes much lower than the amplitude of starspot variability, we confirm the transits with *Spitzer*, conclusively ruling out an instrumental origin for the signal. The *Spitzer* detection of the transits in the near-infrared, at the predicted time and with the same depth as in *TESS* rules out stellar variability as an origin, which should be significantly lower in the *Spitzer* bandpass and should not produce periodic transit-like signals.
2. *DS Tuc A is an eclipsing binary:* Our RV observations showed no variations large enough to be caused by a stellar companion. To test this, we generated 100,000 binaries with random (uniform) mass ratios, argument of periastron, phase, inclination, and eccentricty. The period was fixed at 8.138 days, and inclination was restricted ensure the companion eclipses ($\gtrsim$70°). We then compared each synthetic binary's predicted velocities to the observed velocities assuming an extra jitter term in the velocities of 100 m s^{-1} (from stellar variability). All generated binaries down to 20M_J in mass were rejected at $>5\sigma$, and >99% were rejected down to 5M_J.
3. *Light from a physically unassociated eclipsing binary star or transiting planet system is blended with light from DS Tuc: Spitzer* confirms that the transit signal detected toward DS Tuc A must originate from within a few arcseconds of the star. We detected no stars nearby DS Tuc in our GPI AO imaging, and other groups have previously detected no nearby stars in their own AO observations (Kasper et al. 2007; Vogt et al. 2015). Crucially, due to its proper motion, DS Tuc has moved over half an arcsecond with respect to stationary background sources between the different AO imaging epochs over the last decade, so we are able to definitively rule out background stars too close to DS Tuc A for GPI to resolve.
4. *Light from a physically associated eclipsing binary or planet-hosting companion is blended with light from DS Tuc A:* For this to be true, DS Tuc A must have a binary companion close enough to escape detection by GPI (inside about 8 au) and bright enough to cause the transit signal that we see. The magnitude difference Δm between DS Tuc A and the faintest companion, which could contribute the transit signal, is given by

$$\Delta m \lesssim 2.5 \log_{10}\left(\frac{t_{12}^2}{t_{13}^2 \delta}\right) \quad (2)$$

where t_{12} is the duration of transit ingress/egress, t_{13} is the transit duration from first contact (beginning of ingress) to third contact (beginning of egress), and δ is the observed transit depth (Vanderburg et al. 2019). Fitting the *TESS* light curve with MCMC, but without any constraints from the stellar parameters, yields $\Delta m \lesssim 2.4$ (95% confidence). From a 45 Myr MIST isochrone (Choi et al. 2016; Dotter 2016) at solar metallically (provided in the *TESS* bandpass), this magnitude difference corresponds to a companion star with a mass >0.63 $M_\odot$.

To place a dynamical upper limit on the mass of a companion, we perform a Monte Carlo simulation of companion orbits to DS Tuc A with randomly drawn isotropic inclinations, masses below 1$M_\odot$, and semimajor axes below 8 au (holding the eccentricity to zero). For orbits that produce semimajor amplitudes less than half the range of our RV observations (0.6 km s^{-1}), we find that we can exclude companion masses above 0.28 $M_\odot$ at 95% confidence. The large discrepancy between these mass limits excludes this scenario at high confidence.

Our observational constraints confidently rule out these false-positive scenarios, so DS Tuc Ab is almost certainly a genuine exoplanet.

6. Discussion

6.1. DS Tuc Ab in Context

With an age of $\tau \sim 45$ Myr, DS Tuc Ab is one of the few transiting planets with ages $\tau < 100$ Myr, joining the planets K2-33b (David et al. 2016b; Mann et al. 2016b), V1298 Tau b (David et al. 2019) and AU Mic b (P. Plavchan et al. 2019, in preparation). At $V = 8.5$, DS Tuc A is the brightest of these transiting planet host stars, closely followed by AU Mic at $V = 8.6$.

Using photometry from *TESS* and *Spitzer*, we determined that DS Tuc Ab has a radius of 5.70 ± 0.17 $R_\oplus$, placing it in the sparsely populated realm of super-Neptunes and sub-Saturns. The planet is young enough that it likely still contracting due to internal cooling and may also be losing mass; models from Bodenheimer et al. (2018) suggest that its radius will shrink by 5%–10% over the next few 100 Myr.

DS Tuc is a visual binary, and we find no evidence for additional massive companions in the system. While DS Tuc B has previously been suggested to be a spectroscopic binary, we do not see two components in the spectrum of DS Tuc B at any observed epoch, a visual companion in high-contrast imaging data, or periodic RV variations at the precision of our data (200 m s^{-1}). The detection of planetary or substellar companions orbiting DS Tuc A exterior to DS Tuc Ab could indicate that dynamical interactions played a role in the present orbit of DS Tuc A; however, our high-contrast imaging data from GPI shows no companions with masses more than about 5$M_{\rm Jup}$ between 10 and 80 au.

The orbit of the stellar binary is likely to be closely but not perfectly aligned with both the orbit of the transiting planet and the spin axis of the planet-hosting star. We found a binary orbit inclination of $96.^\circ9 \pm 0.^\circ9$, a planetary inclination of $89.5^{+0.34\,\circ}_{-0.41}$, and a stellar inclination of $i > 82^\circ$ (1σ limit). The latter two quantities use the convention of $i < 90$; however, $i > 90$ is equally likely. Although the PAs are presently unconstrained, the chance of all three having the similar inclinations by chance is small, suggesting that the three axes are in fact close to aligned. This is similar to the five-planet Kepler-444ABC system (Campante et al. 2015). Dupuy et al. (2016) found that the orbit of Kepler-444BC and the orbits of the planets around Kepler-444A have the same inclination angle, and suggested that the planets formed in situ in close orbits around Kepler-444A.

The stellar density that we determine from the transit fit differs from that which we calculate from the stellar parameters

by 3σ. The most likely reason is either errors in the model-derived stellar mass, or a mild eccentricity ($0.05 \lesssim e \lesssim 0.1$). While our mass estimate has formal errors of $\simeq$6%, predictions from different model grids can vary by $\simeq$10%. Moderate eccentricities have been found for some other young planets, including two in the Hyades (Quinn et al. 2014; P. C. Thao et al. 2019, in preparation).

6.2. Prospects for Follow-up

Due to the brightness of DS Tuc A, this system offers an exciting opportunity for detailed characterization of a young planet. Measuring the planetary mass would allow one to compare the planet's density to that of older planets. A distinct possibility is that mass estimates based on field-age planets represent an overestimate for DS Tuc Ab, given that the planet could still retain heat from its formation and might undergo future radius evolution as its atmosphere is sculpted by photoevaporative ultraviolet flux. While these processes would impact the planetary radius, they are not expected to have a substantial impact on the planetary mass.

The Chen & Kipping (2017) mass–radius relation, which is based on field-aged planetary systems, predicts a planetary mass of $28^{+35}_{-13}\,M_{\oplus}$. The expected RV semi-amplitude produced by DS Tuc Ab would then be $9^{+11}_{-4}\,\mathrm{m\,s^{-1}}$. As evidenced by the large error bars on the inferred planet mass, there are relatively few planets with sizes between Neptune and Saturn with measured masses; and the planetary mass–radius relation is poorly constrained for planets of this size.

Measuring the Rossiter–McLaughlin effect would determine the sky-projected angle between the stellar rotational and planetary orbital angular momentum vectors, and test our hypothesis that the stellar spin and planetary orbital axes are aligned. We estimate the RV amplitude due to the Rossiter-McLaughin effect using the relation $\Delta \mathrm{RV} \simeq 0.65\, v \sin i_{*} \left(\frac{R_P}{R_*}\right)^2 \sqrt{1-b^2}$ (Gaudi & Winn 2007), finding a predicted amplitude of $32\,\mathrm{m\,s^{-1}}$. Combining a spin–orbit misalignment measurement from Doppler Tomography (e.g., Johnson et al. 2017) or the Rossiter–McLaughlin effect (e.g., Narita et al. 2010) with our measurement of i_* from the rotation period and $v \sin i_*$, one could measure full 3D spin–orbit misalignment ψ. DS Tuc Ab joins a small number of planets where such measurements are possible.

Measuring RV signals on the scales noted above would be well within reach of current high precision RV instruments, but stellar activity poses a major challenge (e.g., Saar & Donahue 1997; Paulson et al. 2004). DS Tuc A is a very magnetically active star, with $\log R'_{HK} = -4.09$ (Henry et al. 1996). For stars like DS Tuc A, the stellar activity signal on many-day timescales (i.e., over many stellar rotation periods) is expected to be 100–200 $\mathrm{m\,s^{-1}}$ based on the sample of active stars monitored with Keck by Hillenbrand et al. (2015). While a jitter of this level would seem to preclude RV measurements of the planetary signal, stellar activity signals can be mitigated by simultaneously modeling the activity and planetary signals using, e.g., Gaussian processes, a process which would be aided by our knowledge of the star's photometric variability (e.g., Haywood et al. 2014; Rajpaul et al. 2015; López-Morales et al. 2016). It is not clear how well the activity signal can be modeled and removed in an intensive RV campaign to measure a planet's mass or Rossiter–McLaughlin effect.

We investigate prospects for atmospheric characterization with the *James Webb Space Telescope* (*JWST*) by computing its transmission spectroscopy metric using Equation (1) of Kempton et al. (2018). We assume zero albedo and full day-night heat redistribution to estimate an equilibrium temperature for the planet of 850 K. We find a transmission spectroscopy metric is 264, which can be interpreted as the S/N with which its transmission spectrum is expected to be measured (assuming a cloud-free atmosphere) with a 10 hr observing program with the NIRISS instrument. This makes DS Tuc Ab an excellent target for observations with *JWST*. Finally, we note that it may be possible to detect the planetary exosphere, e.g., using He 10830 Å transit observations (Oklopčić & Hirata 2018; Spake et al. 2018).

7. Summary

We report the discovery of a hot planet with a radius of $5.7 \pm 0.17 R_{\oplus}$ around the young star DS Tuc A (G6V, $V = 8.5$) using data from NASA's *TESS* mission. The host star was one of the first identified members of the 45 Myr old Tucana–Horologium association, and has a stellar companion orbiting at $157 < a < 174$ au (1σ interval). The *TESS* data alone were insufficient to validate the planet given the nearby stellar companion, so we used photometry from *Spitzer* to confirm that the planet orbits DS Tuc A and revise the transit parameters. We find that the rotation axis of DS Tuc A, the orbital axis of the stellar binary, and the orbital axis of the planet are likely to be aligned.

This 45-Myr-old planet offers numerous opportunities for further characterization and illustrates the utility of *TESS* in furthering the study of planetary evolution.

The authors would like to thank R. Angus, D. Foreman-Mackey, and B. Sowerwine for helpful conversations regarding this manuscript. This work was supported by the *TESS* Guest Investigator program (grant 80NSSC19K0636, awarded to A.W.M.). E.R.N. acknowledges support from the National Science Foundation Astronomy & Astrophysics Postdoctoral Fellowship Program (Award #1602597). This work makes use of observations from the LCO network. Based on observations obtained at the Southern Astrophysical Research (SOAR) telescope, which is a joint project of the Ministério da Ciência, Tecnologia, Inovações e Comunicações (MCTIC) do Brasil, the U.S. National Optical Astronomy Observatory (NOAO), the University of North Carolina at Chapel Hill (UNC), and Michigan State University (MSU). Some of the observations reported in this Letter were obtained with the Southern African Large Telescope (SALT) through Dartmouth College. This Letter includes data collected by the *TESS* mission, which are publicly available from the Mikulski Archive for Space Telescopes (MAST). Funding for the *TESS* mission is provided by NASA's Science Mission directorate. This research has made use of the Washington Double Star Catalog maintained at the U.S. Naval Observatory. We would like to thank the University of North Carolina at Chapel Hill and the Research Computing group for providing computational resources (the Longleaf Cluster) and support that have contributed to these research results. We acknowledge the use of public *TESS* Alert data from pipelines at the *TESS* Science Office and at the *TESS* Science Processing Operations Center. Resources supporting this work were provided by the NASA High-End Computing (HEC) Program through the NASA Advanced Supercomputing

(NAS) Division at Ames Research Center for the production of the SPOC data products.

Facilities: TESS, SALT (HRS), SOAR (Goodman), WASP, *Spitzer*, LCO (NRES), CDS, MAST.

Software: Astropy, `emcee` (Foreman-Mackey et al. 2013), `celerite` (Foreman-Mackey et al. 2017).

Note added in proof. During the final stages of preparation of this Letter, we learned of an independent analysis done by another team (Benatti et al. 2019).

ORCID iDs

Elisabeth R. Newton https://orcid.org/0000-0003-4150-841X
Andrew W. Mann https://orcid.org/0000-0003-3654-1602
Benjamin M. Tofflemire https://orcid.org/0000-0003-2053-0749
Logan Pearce https://orcid.org/0000-0003-3904-7378
Aaron C. Rizzuto https://orcid.org/0000-0001-9982-1332
Andrew Vanderburg https://orcid.org/0000-0001-7246-5438
Raquel A. Martinez https://orcid.org/0000-0001-6301-896X
Jason J. Wang https://orcid.org/0000-0003-0774-6502
Jean-Baptiste Ruffio https://orcid.org/0000-0003-2233-4821
Adam L. Kraus https://orcid.org/0000-0001-9811-568X
Marshall C. Johnson https://orcid.org/0000-0002-5099-8185
Pa Chia Thao https://orcid.org/0000-0001-5729-6576
Rayna Rampalli https://orcid.org/0000-0001-7337-5936
Eric L. Nielsen https://orcid.org/0000-0001-6975-9056
Karen A. Collins https://orcid.org/0000-0001-6588-9574
Diana Dragomir https://orcid.org/0000-0003-2313-467X
Coel Hellier https://orcid.org/0000-0002-3439-1439
D. R. Anderson https://orcid.org/0000-0001-7416-7522
Thomas Barclay https://orcid.org/0000-0001-7139-2724
Gregory Feiden https://orcid.org/0000-0002-2012-7215
John F. Kielkopf https://orcid.org/0000-0003-0497-2651
Joseph E. Rodriguez https://orcid.org/0000-0001-8812-0565
Chris Stockdale https://orcid.org/0000-0003-2163-1437
Ian A. Waite https://orcid.org/0000-0002-3249-3538
Jack J. Lissauer https://orcid.org/0000-0001-6513-1659
George R. Ricker https://orcid.org/0000-0003-2058-6662
Roland Vanderspek https://orcid.org/0000-0001-6763-6562
David W. Latham https://orcid.org/0000-0001-9911-7388
Joshua N. Winn https://orcid.org/0000-0002-4265-047X
Jon M. Jenkins https://orcid.org/0000-0002-4715-9460
Luke G. Bouma https://orcid.org/0000-0002-0514-5538
Christopher J. Burke https://orcid.org/0000-0002-7754-9486
Michael Fausnaugh https://orcid.org/0000-0002-9113-7162
Koji Mukai https://orcid.org/0000-0002-8286-8094
Steven Villeneuva https://orcid.org/0000-0001-6213-8804
Robert J. De Rosa https://orcid.org/0000-0002-4918-0247
Bruce Macintosh https://orcid.org/0000-0003-1212-7538
Robert A. Wittenmyer https://orcid.org/0000-0001-9957-9304

References

Adams, F. C., Proszkow, E. M., Fatuzzo, M., & Myers, P. C. 2006, ApJ, 641, 504
Allard, F., Homeier, D., & Freytag, B. 2012, RSPTA, 370, 2765
Baraffe, I., Homeier, D., Allard, F., & Chabrier, G. 2015, A&A, 577, A42
Bell, C. P. M., Mamajek, E. E., & Naylor, T. 2015, MNRAS, 454, 593
Benatti, S., Nardiello, D., Malavolta, L., et al. 2019, A&A, submitted (arXiv:1904.01591)
Blackwell, D. E., & Shallis, M. J. 1977, MNRAS, 180, 177
Blunt, S., Nielsen, E. L., De Rosa, R. J., et al. 2017, AJ, 153, 229
Bodenheimer, P., Stevenson, D. J., Lissauer, J. J., & D'Angelo, G. 2018, ApJ, 868, 138
Bonnell, I. A., Smith, K. W., Davies, M. B., & Horne, K. 2001, MNRAS, 322, 859
Bowler, B. P., Liu, M. C., Shkolnik, E. L., & Tamura, M. 2015, ApJS, 216, 7
Brandt, T. D., McElwain, M. W., Turner, E. L., et al. 2014, ApJ, 794, 159
Brown, T. M., Baliber, N., Bianco, F. B., et al. 2013, PASP, 125, 1031
Buckley, D. A. H., Swart, G. P., & Meiring, J. G. 2006, Proc. SPIE, 6267, 62670Z
Campante, T. L., Barclay, T., Swift, J. J., et al. 2015, ApJ, 799, 170
Cannon, A. J., & Pickering, E. C. 1924, AnHar, 99, 1
Cheetham, A. C., Samland, M., Brems, S. S., et al. 2019, A&A, 622, A80
Chen, J., & Kipping, D. 2017, ApJ, 834, 17
Choi, J., Dotter, A., Conroy, C., et al. 2016, ApJ, 823, 102
Clanton, C., & Gaudi, B. S. 2016, ApJ, 819, 125
Claret, A. 2017, A&A, 600, A30
Claret, A., & Bloemen, S. 2011, A&A, 529, A75
Clemens, J. C., Crain, J. A., & Anderson, R. 2004, Proc. SPIE, 5492, 331
Cohen, M., Wheaton, W. A., & Megeath, S. T. 2003, AJ, 126, 1090
Crause, L. A., Sharples, R. M., Bramall, D. G., et al. 2014, Proc. SPIE, 9147, 91476T
Cushing, M. C., Marley, M. S., Saumon, D., et al. 2008, ApJ, 678, 1372
Cutispoto, G., Pastori, L., Pasquini, L., et al. 2002, A&A, 384, 491
David, T. J., Cody, A. M., Hedges, C. L., et al. 2019, AJ, in press (arXiv:1902.09670)
David, T. J., Conroy, K. E., Hillenbrand, L. A., et al. 2016a, AJ, 151, 112
David, T. J., Hillenbrand, L. A., Petigura, E. A., et al. 2016b, Natur, 534, 658
Dotter, A. 2016, ApJS, 222, 8
Dotter, A., Chaboyer, B., Jevremović, D., et al. 2008, ApJS, 178, 89
Dupuy, T. J., Kratter, K. M., Kraus, A. L., et al. 2016, ApJ, 817, 80
Evans, D. W., Riello, M., De Angeli, F., et al. 2018, A&A, 616, A4
Fazio, G. G., Hora, J. L., Allen, L. E., et al. 2004, ApJS, 154, 10
Feiden, G. A. 2016, A&A, 593, A99
Feiden, G. A., & Chaboyer, B. 2014, ApJ, 789, 53
Foreman-Mackey, D., Agol, E., Ambikasaran, S., & Angus, R. 2017, AJ, 154, 220
Foreman-Mackey, D., Hogg, D. W., Lang, D., & Goodman, J. 2013, PASP, 125, 306
Gagné, J., & Faherty, J. K. 2018, ApJ, 862, 138
Gagné, J., Lafrenière, D., Doyon, R., Malo, L., & Artigau, É. 2015, ApJ, 798, 73
Gaidos, E., Mann, A. W., Kraus, A. L., & Ireland, M. 2016, MNRAS, 457, 2877
Gaidos, E., Mann, A. W., Lépine, S., et al. 2014, MNRAS, 443, 2561
Gaudi, B. S., & Winn, J. N. 2007, ApJ, 655, 550
Haywood, R. D., Collier Cameron, A., Queloz, D., et al. 2014, MNRAS, 443, 2517
Henry, T. J., Soderblom, D. R., Donahue, R. A., & Baliunas, S. L. 1996, AJ, 111, 439
Hillenbrand, L., Isaacson, H., Marcy, G., et al. 2015, in 18th Cambridge Workshop on Cool Stars, Stellar Systems, and the Sun, ed. G. T. van Belle & H. C. Harris (Flagstaff, AZ: Lowell Observatory), 759
Hirano, T., Sanchis-Ojeda, R., Takeda, Y., et al. 2012, ApJ, 756, 66
Høg, E., Fabricius, C., Makarov, V. V., et al. 2000, A&A, 355, L27
Horne, K. 1986, PASP, 98, 609
Ingalls, J. G., Krick, J. E., Carey, S. J., et al. 2012, Proc. SPIE, 8442, 84421Y
Ingalls, J. G., Krick, J. E., Carey, S. J., et al. 2016, AJ, 152, 44
Jarrett, T. H., Cohen, M., Masci, F., et al. 2011, ApJ, 735, 112
Jenkins, J. M. 2015, BAAS, 3, 106.05
Jenkins, J. M., Twicken, J. D., McCauliff, S., et al. 2016, Proc. SPIE, 9913, 99133E
Johnson, J. A., Apps, K., Gazak, J. Z., et al. 2011, ApJ, 730, 79
Johnson, M. C., Cochran, W. D., Addison, B. C., Tinney, C. G., & Wright, D. J. 2017, AJ, 154, 137
Johnson, M. C., Dai, F., Justesen, A. B., et al. 2018, MNRAS, 481, 596
Kasper, M., Apai, D., Janson, M., & Brandner, W. 2007, A&A, 472, 321
Kempton, E. M.-R., Bean, J. L., Louie, D. R., et al. 2018, PASP, 130, 114401
Kipping, D. M. 2013, MNRAS, 435, 2152
Kiraga, M. 2012, AcA, 62, 67
Kniazev, A. Y., Gvaramadze, V. V., & Berdnikov, L. N. 2016, MNRAS, 459, 3068
Kniazev, A. Y., Gvaramadze, V. V., & Berdnikov, L. N. 2017, in ASP Conf. Ser. 510, Stars: From Collapse to Collapse, ed. Y. Balega et al. (San Francisco, CA: ASP), arXiv:1612.00292
Kovács, G., Zucker, S., & Mazeh, T. 2002, A&A, 391, 369
Kraus, A. L., Shkolnik, E. L., Allers, K. N., & Liu, M. C. 2014, AJ, 147, 146

Kreidberg, L. 2015, PASP, 127, 1161
Lindegren, L., Hernández, J., Bombrun, A., et al. 2018, A&A, 616, A2
Livingston, J. H., Dai, F., Hirano, T., et al. 2019, MNRAS, 484, 8
Lopez, E. D. 2017, MNRAS, 472, 245
López-Morales, M., Haywood, R. D., Coughlin, J. L., et al. 2016, AJ, 152, 204
Macintosh, B., Graham, J. R., Ingraham, P., et al. 2014, PNAS, 111, 12661
Maíz Apellániz, J., & Weiler, M. 2018, A&A, 619, A180
Mandel, K., & Agol, E. 2002, ApJL, 580, L171
Mann, A. W., Feiden, G. A., Gaidos, E., Boyajian, T., & von Braun, K. 2015, ApJ, 804, 64
Mann, A. W., Gaidos, E., Mace, G. N., et al. 2016a, ApJ, 818, 46
Mann, A. W., Gaidos, E., Vanderburg, A., et al. 2017, AJ, 153, 64
Mann, A. W., Newton, E. R., Rizzuto, A. C., et al. 2016b, AJ, 152, 61
Mann, A. W., & von Braun, K. 2015, PASP, 127, 102
Marois, C., Lafrenière, D., Doyon, R., Macintosh, B., & Nadeau, D. 2006, ApJ, 641, 556
Martinez, R. A., & Kraus, A. L. 2019, AJ, in press (arXiv:1907.06767)
Morton, T. D., & Winn, J. N. 2014, ApJ, 796, 47
Muirhead, P. S., Becker, J., Feiden, G. A., et al. 2014, ApJS, 213, 5
Narita, N., Hirano, T., Sanchis-Ojeda, R., et al. 2010, PASJ, 62, L61
Nielsen, E. L., De Rosa, R. J., Macintosh, B., et al. 2019, AJ, 158, 13
Oklopčić, A., & Hirata, C. M. 2018, ApJL, 855, L11
Owen, J. E., & Lai, D. 2018, MNRAS, 479, 5012
Owen, J. E., & Wu, Y. 2017, ApJ, 847, 29
Paulson, D. B., Cochran, W. D., & Hatzes, A. P. 2004, AJ, 127, 3579
Pearce, L. 2019, Logan's OFTI, v1.0.0 Zenodo, doi:10.5281/zenodo.2619579
Pearce, L. A., Kraus, A. L., Dupuy, T. J., et al. 2019, AJ, 157, 71
Pepe, F., Mayor, M., Galland, F., et al. 2002, A&A, 388, 632
Pollacco, D. L., Skillen, I., Collier Cameron, A., et al. 2006, PASP, 118, 1407
Quinn, S. N., White, R. J., Latham, D. W., et al. 2012, ApJL, 756, L33
Quinn, S. N., White, R. J., Latham, D. W., et al. 2014, ApJ, 787, 27
Rajpaul, V., Aigrain, S., Osborne, M. A., Reece, S., & Roberts, S. 2015, MNRAS, 452, 2269
Rayner, J. T., Cushing, M. C., & Vacca, W. D. 2009, ApJS, 185, 289
Ricker, G. R., Winn, J. N., Vanderspek, R., et al. 2014, Proc. SPIE, 9143, 914320
Rizzuto, A. C., Mann, A. W., Vanderburg, A., et al. 2017, AJ, 154, 224
Rizzuto, A. C., Vanderburg, A., Mann, A. W., et al. 2018, AJ, 156, 195
Ruane, G., Ngo, H., Mawet, D., et al. 2019, AJ, 157, 118
Rucinski, S. M. 1992, AJ, 104, 1968
Ruffio, J.-B., Macintosh, B., Wang, J. J., et al. 2017a, ApJ, 842, 14
Ruffio, J.-B., Macintosh, B., Wang, J. J., & Pueyo, L. 2017b, Proc. SPIE, 10400, 1040027
Saar, S. H., & Donahue, R. A. 1997, ApJ, 485, 319
Sfeir, D. M., Lallement, R., Crifo, F., & Welsh, B. Y. 1999, A&A, 346, 785
Siverd, R. J., Brown, T. M., Barnes, S., et al. 2018, Proc. SPIE, 10702, 107026C
Skrutskie, M. F., Cutri, R. M., Stiening, R., et al. 2006, AJ, 131, 1163
Soderblom, D. R., King, J. R., & Henry, T. J. 1998, AJ, 116, 396
Soummer, R., Pueyo, L., & Larkin, J. 2012, ApJL, 755, L28
Spake, J. J., Sing, D. K., Evans, T. M., et al. 2018, Natur, 557, 68
Sparks, W. B., & Ford, H. C. 2002, ApJ, 578, 543
Spina, L., Randich, S., Palla, F., et al. 2014, A&A, 568, A2
Spurzem, R., Giersz, M., Heggie, D. C., & Lin, D. N. C. 2009, ApJ, 697, 458
Stassun, K. G., Oelkers, R. J., Pepper, J., et al. 2018, AJ, 156, 102
Torres, C. A. O., da Silva, L., Quast, G. R., de la Reza, R., & Jilinski, E. 2000, AJ, 120, 1410
Torres, C. a. O., Quast, G. R., da Silva, L., et al. 2006, A&A, 460, 695
Torres, G. 1988, Ap&SS, 147, 257
Vanderburg, A., Huang, C. X., Rodriguez, J. E., et al. 2019, arXiv:1905.05193
Vogt, N., Mugrauer, M., Neuhäuser, R., et al. 2015, AN, 336, 97
Wang, J. J., Perrin, M. D., Savransky, D., et al. 2018, JATIS, 4, 018002
Wang, J. J., Ruffio, J.-B., De Rosa, R. J., et al. 2015, pyKLIP: PSF Subtraction for Exoplanets and Disks, Astrophysics Source Code Library, ascl:1506.001
Winn, J. N., Petigura, E. A., Morton, T. D., et al. 2017, AJ, 154, 270
Wright, E. L., Eisenhardt, P. R. M., Mainzer, A. K., et al. 2010, AJ, 140, 1868
Zuckerman, B., & Webb, R. A. 2000, ApJ, 535, 959